PAPER

Investigation of carbon ionization in HiPIMS discharge with a hollow cathode magnetron

View the article online for updates and enhancements.

Investigation of carbon ionization in HiPIMS discharge with a hollow cathode magnetron

N P Poluektov[1,*] , I I Usatov[1] and M Yu Kladov[2]

[1] Bauman Moscow State Technical University, Mytishchi, Moscow region, 141005 Russia
[2] JSC 'Kompozit', Korolev, Moscow region 141070, Russia

E-mail: poluekt@mgul.ac.ru and maksim.kladov@gmail.com

CrossMark

Abstract

Study of HiPIMS neon plasma produced by the hollow graphite cathode magnetron was carried out. The pressure is 2.66 Pa and average discharge power is up to 490 W. The emission spectra in the UV spectral regions shows strong lines of carbon and neon ions. The dynamics of the intensities of C^+ and C lines and their dependency on the discharge power were measured through the side window at a distance of 12 cm from the cathode. Using probe measurements, the plasma parameters inside and outside a hollow cathode magnetron (HCM) with discharge have been determined. The plasma density reaches 1.5×10^{12} cm^3 and the electron temperature is 6 eV at a distance of 12 cm. The EEDF shows the presence of electrons with energy up to 32 eV. The goal of this research is to investigate the carbon ionization in the HiPIMS discharge with a HCM.

Keywords: hollow cathode magnetron, HiPIMS, carbon ionization

(Some figures may appear in colour only in the online journal)

1. Introduction

Hydrogen-free diamond-like carbon (DLC) is a versatile material, which exhibits excellent mechanical, electrical and optical properties [1, 2]. Due to these features, DLC films are widely used for surface protection in cutting tools [3], magnetic storage disks [4], biomedical devices [5], antireflection coatings, and optical sensors [6]. The properties of DLC thin films are determined by the bonding configuration (sp^3/sp^2 fraction) of its carbon atoms. Hard hydrogen-free DLC films with a large number of carbon sp^3 bonds are designated as tetrahedral amorphous carbon (ta-C) films. DLC films exhibiting these properties are usually produced by highly ionized physical vapor deposition (PVD) techniques, such as filtered cathodic arc (FCA) or pulsed laser deposition (PLD) [7–10]. In PVD techniques, the ions of inert gas (Ar, Ne) and carbon are accelerated by substrate bias voltage. A highly ionized deposition flux provides means for controlling the energy of the depositing atoms that makes it possible to synthesize DLC with desired properties. The resulting DLC films typically exhibit a high density (2.8–3.2 g cm^{-3}) together with a high sp^3 bond fraction (75%–90%), which entails a significantly high hardness (>20 GPa). However, coatings deposited by PLD or FCA exhibit high defect densities and surface roughnesses, for example caused by emitted particles from the target, so-called droplets.

High power impulse magnetron sputtering (HiPIMS) discharge allow the creation of comparable ion fluxes of buffer gas on large substrate surface. However, the ionization rate of sputtered carbon species in magnetron sputtering glow plasmas is low because of a low sputtering yield, a high ionization energy (11.3 eV) and a smaller electron impact cross-section as compared to metals. It is well known that sputtered carbon species are difficult to ionize. The reaction rate constant for carbon is lower by two to three orders than for other metals such as titanium and copper [11, 12]. In addition, hard hydrogen-free DLCs are synthesized by highly ionized plasma suffer from large compressive stresses that limit their applicability [13].

Despite the difficulties, the HiPIMS discharges are intensively studied to produce of ta-C films [14–19]. The use of

---

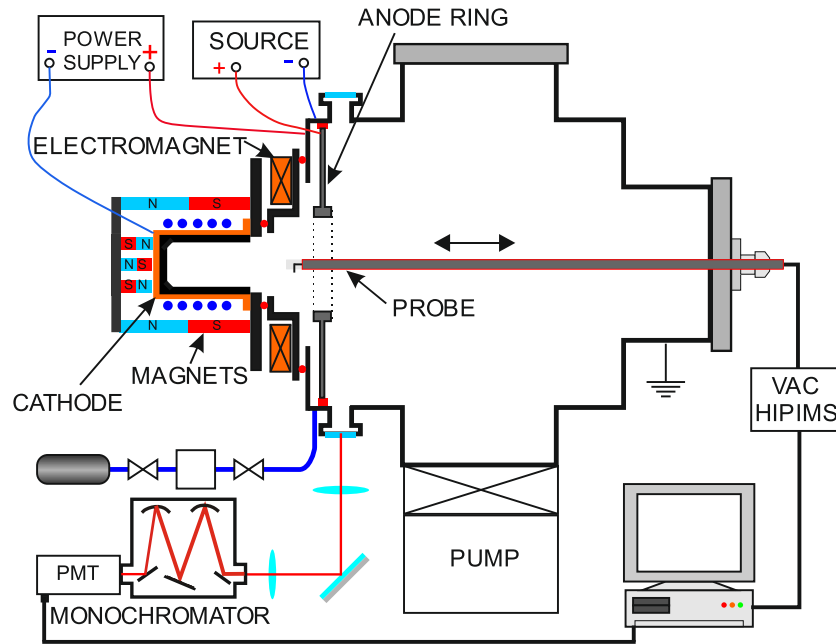* Author to whom any correspondence should be addressed.
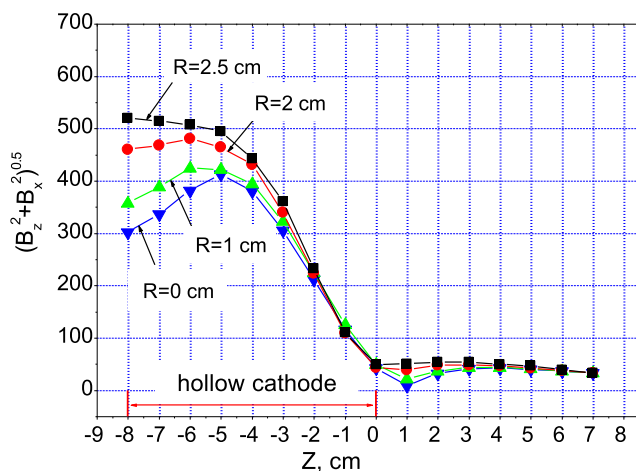
Figure 1. The experimental setup.

Figure 2. Magnetic field of a hollow cathode magnetron measured in the middle section. $I_{el} = 0.9$ A.

Ne as sputtering gas significantly increases the ionization of sputtered C compared to standard Ar-HiPIMS discharges and allows to obtain carbon films with a high mass density [13, 20, 21]. Neon has a higher ionization energy ($E_i = 21.56$ eV) than Ar ($E_i = 15.6$ eV). The electron temperature increases, which follows from the electron energy balance. This in turn increases the ionization rate coefficient, which exponentially depends on the electron temperature. As a result, DLC films with a high mass density of 2.7 g cm^{-3} and low compressive stresses (2.5 GPa) were produced [13].

There are few studies of plasma parameters during sputtering of a graphite target [20, 22]. In this work, we studied the properties of a Ne-HiPIMS discharge produced by a hollow cathode magnetron (HCM) with a graphite target. Previous experiments with Cu target showed that the plasma density in this discharge remains high ($>10^{12}$ cm^{-3} at a pressure of 1.33–2.66 Pa up to a distance of 20 cm from the magnetron [23]. This is a significant difference of the HCM from discharges with a planar cathode, in which regions with the maximum densities are located close to the cathode surface. The goal of this research is to investigate the carbon ionization in the HiPIMS discharge with the HCM.

2. Experimental apparatus

The experimental setup of the magnetron discharge with a hollow cathode is shown in figure 1. The cathode consists of a cup-shaped C target (purity 99.9%) (internal diameter 6 cm, length 8 cm) installed in copper water cooled cylinder. Plasma from the cathode diffuses into a reactor (30 cm diameter, 45 cm length). The electrically insulated insert of 18 cm internal diameter and 7 cm in length is located between the cathode and plasma chamber. The chamber was pumped to base pressure 10^{-3} Pa using a diffusion pump. Ne was used as process gas. Pressure was measured using Baratron pressure gauge. Gas flow (25 sccm) is provided by the gas flow controller. The magnetic field is produced by eight columns of Nd–Fe–B magnets surrounded the target with ring iron flanges on the edges. Magnets are also installed behind the bottom of the cathode. Their distance to the plasma is 1 cm and their effect on the discharge is rather weak. The downstream of the HCM is located the electromagnet. Its magnetic field is

directed against the magnetic field of the permanent magnets. The plasma flow expends to more a uniform radial distribution when the electromagnet is on. The magnetic mirror formed by this system confines secondary electrons inside the cathode. Figure 2 shows the magnetic field of a HCM measured by a triple Hall sensor in the middle section.

The anode of discharge is a copper ring (i.d. = 15 cm) positioned at distance of 10 cm from the cathode insulated from chamber. In the experiments described below, a voltage U_{an} of $+40 \div 60$ V was applied to the ring anode from additional source; in this case, the anode collected $(0.7 \div 0.8)$ part of the total discharge current.

Home-made a high power pulse supply was capable of delivering 900 V and 200 A peak values. A low inductance resistor of 3 Ω was used to limit the plasma current. The discharge was ignited using a preionization system based on a dc source (2 kV, 5–25 mA), and then the pulsed source was switched on. The DC power supply ensured the discharge repeatability. The discharge voltage between pulses was self-regulated in the range of 250–400 V, depending on the pressure and magnetic field.

The discharge voltage and current were measured by a high voltage probe (P39258, Holden Electronics) and a current sensor CSNB121 (Honeywell) were recorded by a two-channel digital oscilloscope Bordo 421 (150 MHz).

The plasma emission was monitored through a side quartz window (i.d. = 5 cm) located at a distance of 12 cm from the HCM. Spectra of plasma emission were measured by a grating monochromator (inverse dispersion of 1.3 nm mm^{-1}) equipped with a photomultiplier tube. The hardware and software for processing spectral data allows to record the plasma emission spectra at different times during the discharge.

Using the developed time-resolved Langmuir probe measurements it was possible to determine the temporal evolution of plasma parameters. The tungsten Langmuir probes were 0.2 mm in diameter and 2 mm in length. The probe bias voltages U_p can be scanned from -80 to $+80$ V in voltage steps of 0.2 V. The maximum obtainable current was 500 mA. The hardware components of the system include the high-power voltage amplifier developed in our laboratory, the sample storage system, the current and voltage detectors, and the PCI card National Instruments NI6221 with three 16-bit ADC, two 16-bit DAC, and multiplexer. The maximum number of pairs of voltage–current points in the I–V characteristic of the probe is 540, and each pair being obtained by averaging over 10 measurements. Processing of the measured I–V characteristic includes smoothing of the data by means of cubic splines or the Savitzky–Golay filter and calculation of the first and second current derivatives by the method proposed in [24]. The first derivative was used to determine plasma potential Vs, while the second derivative was used to determine the electron energy distribution function (EEDF). The electron density was determined by integrating the EEDF over energy. We also used a planar probe diameter of 13 mm to measure the ion saturation current density.
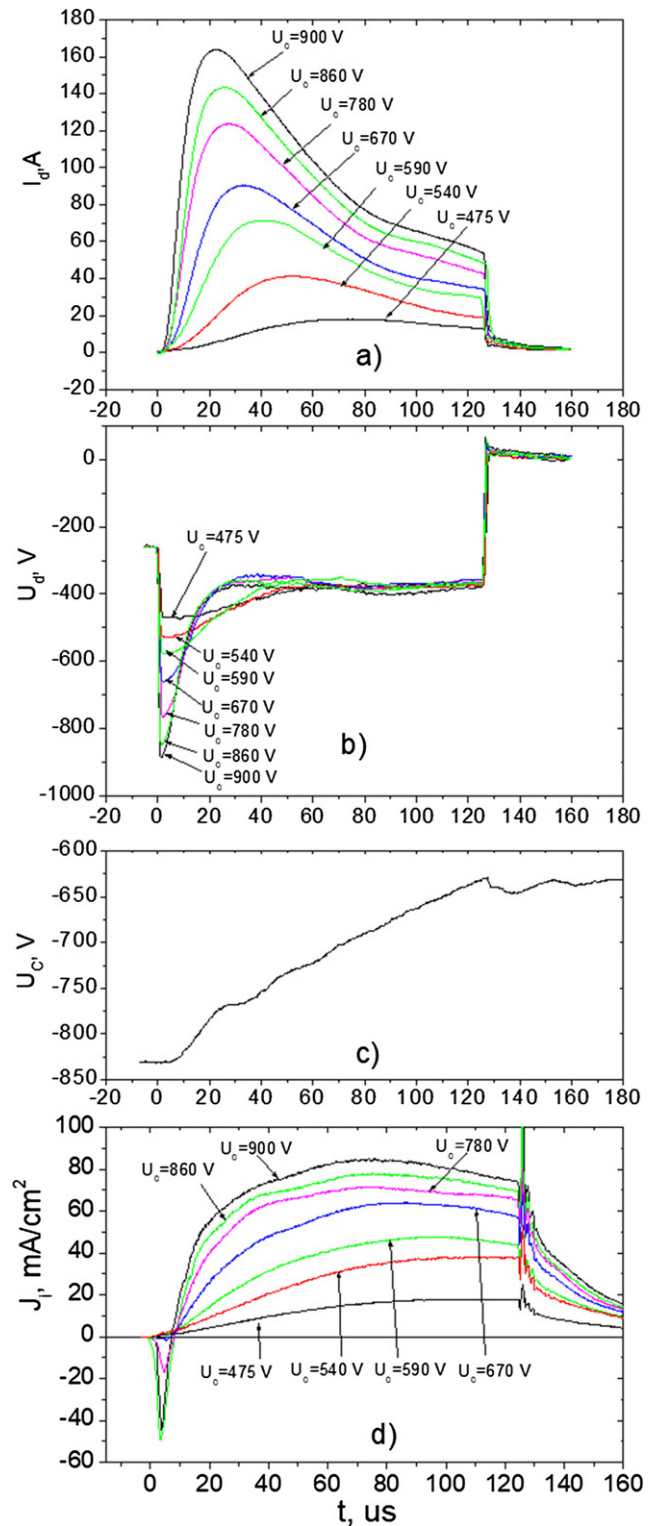

Figure 3. Waveforms of the discharge current (a), voltage (b), source capacitor bank voltage (c), ion current density J_i at $z = 12$ cm (d). 2.66 Pa, $I_{el} = 0.9$ A, $U_{an} = 40$ V.

No doubly charged ions were observed. Since the probe is located in bulk plasma, the plasma is quasi-neutral there and therefore the electron density is equal to the ion density. The

ion density is the ion neon density as the carbon ion density is an order of magnitude smaller.

The electron effective temperature T_e is determined as mean kinetic energy of electron gas:

$$T_e = \frac{2}{3} \frac{\int\limits_0^\infty E f(E) \mathrm{d}E}{\int\limits_0^\infty f(E) \mathrm{d}E}. \tag{1}$$

Here, E is the kinetic energy of the electron gas.

3. Results

Figures 3(a) and (b) show the typical current I_d and voltage U_d traces from the HiPIMS discharge when the capacitor bank (40 μF) was charged to 475–900 V. Other discharge parameters were the pressure $p = 2.66$ Pa, pulse duration of 125 μs, $f = 100$ Hz. The target voltage drops from the source voltage to a constant value of -400 V, which is independent of the initial applied voltage. The initial voltage of -250 V is the voltage of the preionization discharge. The current peak gradually increases with increasing applied voltage, and then decreases. We considered two reasons for the decrease in current. The first is the depletion of the capacitor bank, which is accompanied by a decrease in the discharge voltage U_d after 20 μs. The voltage U_d is the voltage between the cathode and anode. The source capacitor bank voltage (c = 40 μF) is equal to $U_C = U_d + U_R$, where U_R is a voltage drop across the current limiting resistance of 3 Ohms. By the time of the current peak, the exhausted energy is less than 10% of the initial capacity energy and cannot be the reason for the decrease in current. This is true for all initial voltages shown in figure 1(a). However, the shape of the current changes significantly when going to high currents. Figure 3(c) shows the capacitor voltage U_C trace measured by a high voltage probe, which confirms our estimations.

Another reason for the decrease in the discharge current is the rarefaction. We suppose that the rarefaction effect due to collision with sputtering carbon atoms is small because of the low sputtering yield of carbon. The rarefaction may also be due to from ion-produced neutrals reflected from the target and an increase in the buffer gas temperature, which can exceed 1000 K [25, 26], but the main reason of this effect is the ionization of neon atoms.

The constant voltage of the target means that there is no difference in the sputtering yield per bombarding ion. Therefore, the density of the sputtered species is proportional to the target current, assuming that the target current is proportional to the plasma density. The shape of the current indicates that there is no self-sputtering.

Figure 3(d) shows the dynamics of the ion saturation current density I_i as a function of the discharge current. The current was measured with a planar probe located at a distance of 12 cm from the HCM on the axis. Bias voltage was -60 V. The ion current is proportional to the discharge current, and at $I_d = 160$ A, the ion current density reaches 85 mA cm^{-2}. Magnetic fields of electromagnets can be changed to control the
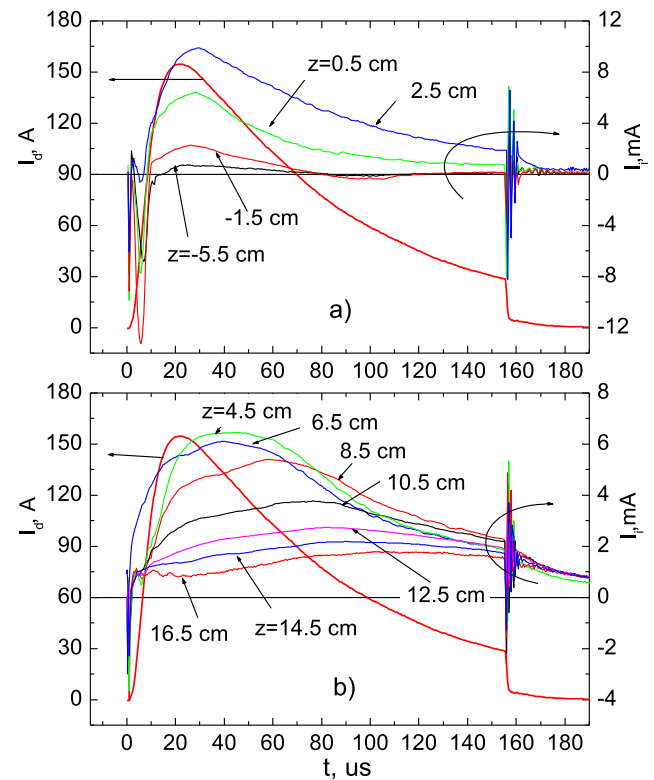

Figure 4. (a) and (b) Dynamics of the ion saturation current at different distances along the discharge axis. (a) Inside and near the exit of the HCM, (b) outside the HCM. $p = 2.26$ Pa, $I_d = 150$ A, $I_{el} = 0.9$ A, $U_{an} = 40$ V.

radial plasma uniformity and I_i on the axis increases 1.5 times when $I_{el} = 0.6$ A.

At peak current $I_d = 160$ A the discharge energy E is 4.9 J, the discharge power averaged over the pulse ($\tau = 125$ μs) is $P_{pulse} = 39.2$ kW, and the power averaged over the pulse period (10 ms) is $P_{av} = 490$ W. The erosion zone is located in the corner at the bottom of the target and on the cylindrical surface of the hollow cathode. The effective racetrack area is about 150 cm^2. The peak current density is 1.1 A cm^{-2}, the peak power density is 0.4 kW cm^{-2} and average power density is 3.3 W cm^{-2}.

Figures 4(a) and (b) show the dynamics of the ion saturation current measured by the probe ($U_p = -60$ V) at different distances along the discharge axis. ($R = 0$ cm). The edge of the cathode has the coordinate $Z = 0$. From the figure 4 follows that, at times $0 < t < 10$ μs, the current is negative due to high-energy electrons arising from the breakdown. The number of high-energy electrons is large in the depth of the hollow cathode and decreases with increasing distance due to collisions with atoms. A longitudinal magnetic field created by the solenoid promotes the propagation of electrons and the probe detects them at a large distance from the cathode.

The formation of a negative current pulse on the probe is quite typical during the first several microseconds for the HiPIMS discharge.

The ion current at $t > 10$ μs increases and its peak coincides with the peak of the discharge current (figure 4(a)).

The ion current is small at the hollow cathode bottom and grows toward the exit. The peak value of the ion current near the exit is 9 times greater than that of at the bottom. After 60 μs, the current inside the cathode decreases to zero until the end of the discharge. Thus, the plasma density on the axis inside the hollow cathode is low during the discharge.

The plasma with high density within the hollow cathode is located near the side surface. Probe measurements showed that the ion current increases with a higher radius and at $R = 2$ cm and $z = -3$ cm is 10 times the current on the axis. A detailed discussion of these measurements is beyond the scope of this paper. A similar result was obtained in a DC HCM 14 cm in diameter, where probe measurements were made inside the cathode at different radii [27].

It is interesting to note that the picture is different for a discharge in argon. The ion current at $R = 0$ cm within HCM, although small, does not fall to zero and the current peak ratio I_{i_exit}/I_{i_bottom} is 4. Recalling that these results are valid for the case when magnets behind the bottom HCM have little effect on the discharge.

Along axis the ion current outside the hollow cathode increases and its peak is reached at a distance of 2 cm from the magnetron. A similar pattern was observed in the HCM operating in direct current mode [27]. The peak value of the ion current outside the HCM ($z = 2.5$ cm) is 13 times greater that of at the cathode bottom.

Figure 5(a) presents the dynamics of the ion saturation current at different radii measured by a probe at the distance of 12 cm from HCM. The time evolution of the radial ion current distribution plotted from the data in figure 5(a) is shown in figure 5(b). It gives information about ion fluxes onto the substrate. Two ion peaks are clearly observed at radii greater than 1.5 cm. The first peak coincides in time with the discharge current maximum. It is attributed to neon ions produced in the early stages of the discharge by the ionization front generated by the fast electrons crossing the target to the anode ring. The magnitude of the first peak increases with increasing radius (figure 5(b), 20 μs). During 10–20 μs, the current flows along radii of 3–7 cm from the cylindrical surface of the cathode to the anode ring. At 50–60 μs, the ion current at these radii decreases and then slowly rises to a second maximum. The ion current near the axis at $t > 30$ μs, also increases and exceeds the current at the periphery. The second peak is caused by the flux of ions from the hollow cathode. When the discharge voltage drops, the retarding potential for ions decreases and ions leaving the hollow cathode. The second maximum was observed quite often in discharges with a planar cathode [28, 29]. Near the discharge axis, the first and second peaks of ion current overlap (figure 5(a)). The average ion velocity near the axis is greater than at the periphery. Thus, the radial plasma distribution outside the hollow cathode changes during the discharge impulse. The doughnut shape transfers to central core mode. There is the region with null magnetic field at the axis near the exit of the magnetron through which electrons can pass to the substrate. The transverse magnetic field at a larger radius in this place prevents most electrons from escaping.
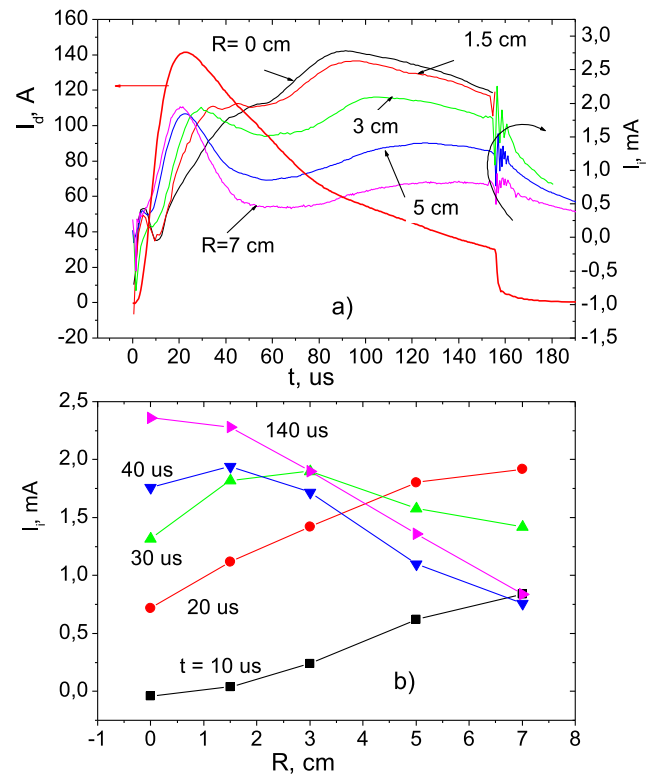

Figure 5. (a) Dynamics of the ion saturation current at different radii for $z = 12$ cm; (b) temporal evolution of radial ion current distribution. 2.66 Pa, $I_{el} = 0.9$ A, $U_{an} = 40$ V.

After the current pulse is switched off ($t = 125$ μs), the plasma density decreases exponentially with a time constant of ≈ 100 μs; then, due to the preionization system, the plasma density remains at a level of $10^9–10^{10}$ cm^{-3} until the beginning of the next pulse (10 ms).

Figure 6 shows the emission spectrum in the UV and blue–green spectral regions of the pulsed discharge plasma measured through the side window at $z = 12$ cm at 60 μs of the discharge. These spectral regions were chosen because they contain the lines of neon and carbon ions. The spectrum shows strong lines of carbon and neon ions. In particular, the intensity carbon ion line C$^+$ 283.7 nm (energy excitation $E_t = 16.33$ eV) is comparable to the intensity of neon ions lines of ($E_t = 31$ eV) and exceeds the intensity of atomic lines C 247.8 nm ($E_t = 7.7$ eV). Nevertheless, it should be noted the discharge color is red, which is due to strong emission of the neon atom lines with $\lambda > 580$ nm. The spectral line intensity $J(\nu_{ij})$ in optically thin plasma is:

$$J(v_{ij}) = K_{ij}n_e n_g \int\limits_{E_t}^{\infty} \sigma v f(E)\,dE, \qquad (2)$$

where σ is the velocity-dependent cross section for electron impact excitation, $f(E)$ is the EEDF, v is the electron velocity, E and E_t represent the electron energy and the excitation threshold.

The lifetime of excited atoms and ions is several 10^{-8} s and during this time they travel a distance of less than 1 mm. This
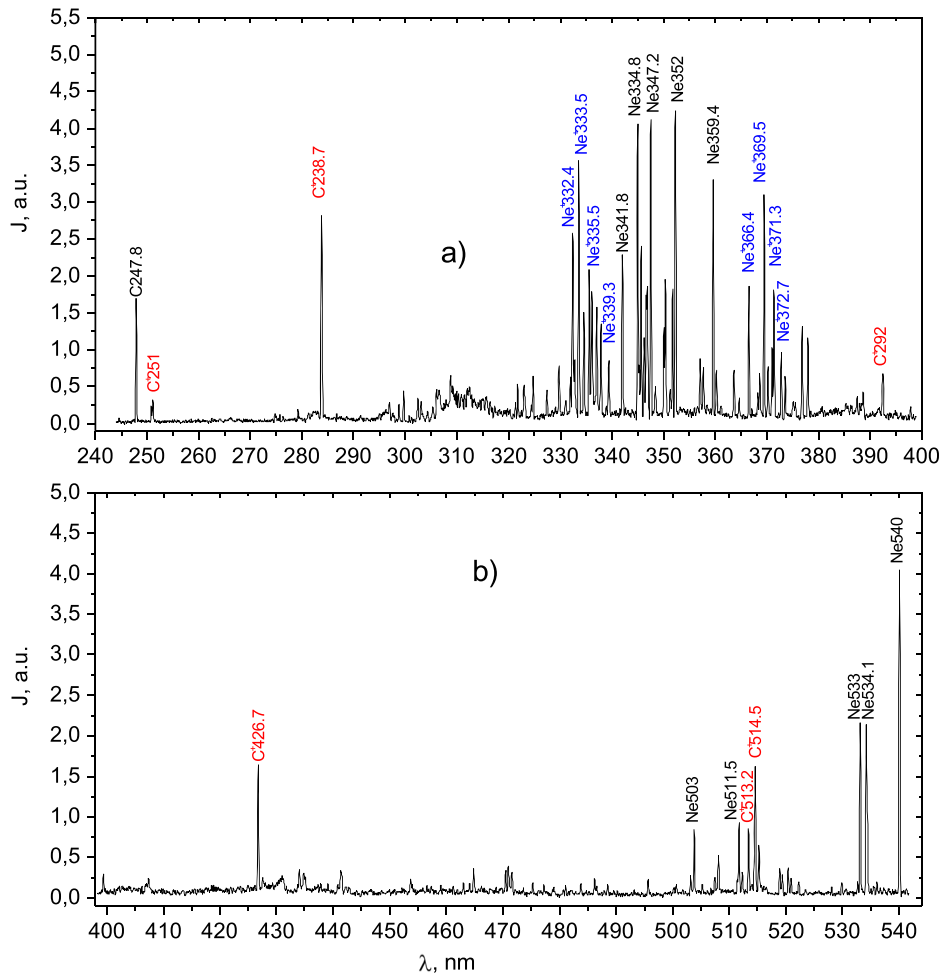
Figure 6. Plasma emission spectra of the HiPIMS discharge at 60 μs of the discharge. $z = 12$ cm, 2.26 Pa, $I_d = 165$ A, $I_{el} = 0.9$ A, pulse duration $\tau = 125$ μs.

means that the radiation of these particles is characteristic for the plasma at the measurement location.

For spectral line C^+ 238.7 nm, electrons should have an energy of $E_t = 16.33$ eV when an excited state is created by the electron impact from the ground state of carbon ion and $E_i + E_t = 27.59$ eV, if the excitation occurs from the ground state of carbon atom. For spectral line Ne^+ 334.5 nm, electrons should have an energy greater than 30.9 eV. Strong lines of carbon and neon ions indicate the presence of electrons with high density and energy downstream the hollow cathode. These measurements confirm the results [23], where the optical probe detected a steep increase of Ar^+ and Cu^+ the emission intensity outside of the HCM.

Figure 7 shows the dynamics of emission of the spectral lines of neon and carbon atoms and ions measured at a distance of 12 cm from the cathode. The emission of Ne atom (352 nm) reaches a peak of 13 μs earlier than maximum current ($t = 21$ μs), then falls to a small value due to ionization. Using optical emission spectrometry Vlček *et al* [30] see almost an order of magnitude decrease in the density of atomic argon due to ionization.

The intensity of the emission of the Ne^+ (334 nm) lines has two peaks. The first peak at $t = 20$ μs corresponds to the

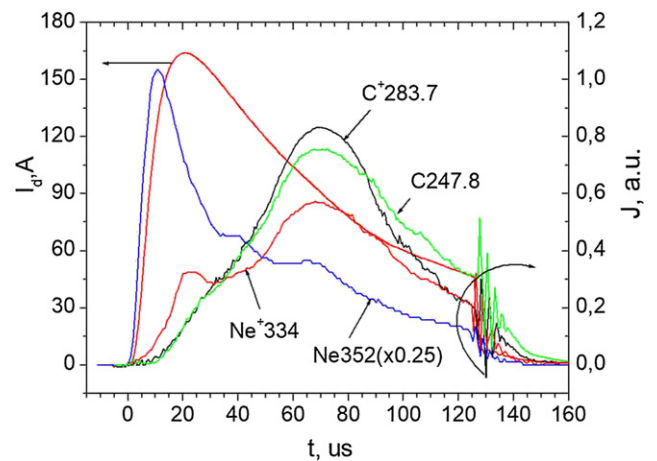**Figure 7.** Dynamics of the discharge current I_d and intensities J of Ne and C atom and ion lines. $z = 12$ cm. $p = 2.66$ Pa, $I_{em} = 0.9$ A.

breakdown and well correlates with a drop intensity of neon atoms. The second peak at 68 μs caused by the diffusion of ions from the cathode.

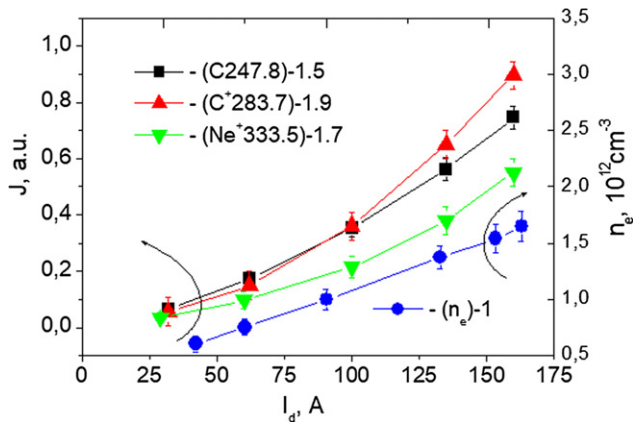The emission of C atoms and ions begins with a delay of several microseconds and reaches a peak of 70 μs.

Figure 8. The peak intensities of the C^+ (283.7 nm), C (247.8 nm), Ne^+ (233.5 nm) spectral lines and the electron density n_e as function of discharge current. $z = 12$ cm. $p = 2.66$ Pa, $I_{em} = 0.9$ A, $\tau = 125$ μs.

The results of probe and spectral measurements presented in figures 4, 5 and 7 agree well with one another and provide information on the dynamics of ionization processes in the pulsed magnetron discharge.

Figure 8 presents the peak intensities J of the C^+ (283.7 nm), C (247.8 nm) and Ne^+ (333.5 nm) lines as function of discharge current. The numbers behind brackets indicate the exponent in a power law. Since these lines are close to each other, the photomultiplier sensitivity is equal for them.

The emitted intensity of C atom exceeds intensity of C^+ for discharge current less than 100 A, then with increasing current the situation is reversed. The $J(C^+)/J(C)$ ratio increases with decreasing discharge pressure and at 1.33 Pa the C^+ (283.7 nm) intensity is about two times higher than C (247.8 nm) intensity at a current of 160 A. The emitted intensity $J(C^+)$ rises faster than $J(Ne^+)$ with increasing discharge current. This should increase the ratio of carbon ion density to neon ion density.

The work [31] considers mechanism for the production of excited atoms and ions of buffer gas and target in a high density plasma. It was shown that the ion emitted intensity $J(\text{ion}) \propto n_e^2$, if main ionization occurs by an electron impact from the ion ground state and dominant loss is due to diffusion. In our case, this mechanism is similar, since the exponent is close to 2.

Figure 8 shows also the dependence of the electron density n_e on the discharge current obtained by Langmuir probe at 70 μs of the discharge at a distance $z = 12$ cm from HCM. It can be seen that the plasma density increases linearly with the discharge current and at $I_d = 160$ A reaches $n_e = 1.5 \times 10^{12}$ cm^{-3}. Thus, an increase of electron density with power rise causes effective ionization of the sputtered C atoms.

Figure 9(a) shows the axial distributions of the electron density n_e on the discharge axis at 40 μs of the discharge, obtained from the probe I–V characteristic. Note that the discharge current is 60 A. Probe measurements are limited to a density of 3×10^{12} cm^{-3} since the large electronic saturation current
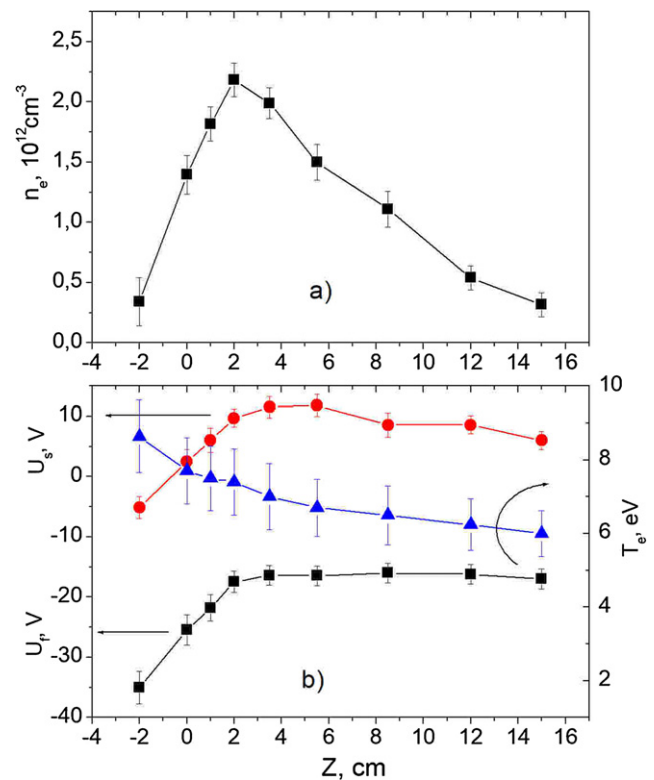

Figure 9. Axial distributions of the electron density n_e (a); floating U_f, plasma U_s potentials and electron temperature T_e (b) at 40 μs of the discharge. $p = 2.66$ Pa, $I_d = 60$ A, $I_{em} = 0.9$ A, $U_{an} = 40$ V, $\tau = 125$ μs.

exceeds the amplifier output current. Inside the magnetron, the electron density on the axis decreases sharply, which agrees with the results of the ion current measurements in figure 4(a). A similar result was obtained from two-dimensional computational investigation of the HCM at a certain position of the magnetic cusp [32]. The maximum density ($n_e > 2 \times 10^{12}$ cm^{-3}) was observed at distances of $2 \div 3$ cm from the magnetron output. At a distance of 12 cm, it decreases to 0.5×10^{12} cm^{-3}.

Figure 9(b) presents the axial distributions of the floating U_f and plasma U_s potentials and temperature T_e at 40 μs of the discharge. The plasma potential increases linearly from -5 V to $+10$ V at the output of the cathode (-2 cm $< z < 2$ cm). We see that an electric field of 3.8 V cm^{-1} exists in this region. This distribution acts as a potential barrier for ions, which prevents them from leaving the cathode. At large distances, the plasma potential changes little. As will be shown later large ionization of the sputtered C atoms occurs in the region $z > 0$ cm, where the plasma density peak is located.

Figure 9(b) also shows the axial distributions of the electron temperature T_e on the discharge axis at 40 μs of the discharge. The electron temperature decreases with a distance from the cathode from 9 eV at $z = -2$ cm to 6 eV at $z = 15$ cm. This temperature distribution changes only slightly during the discharge.

Introducing the probe into the hollow cathode along an axis does not cause a perturbation of the discharge. The current and voltage traces do not change. This is true for
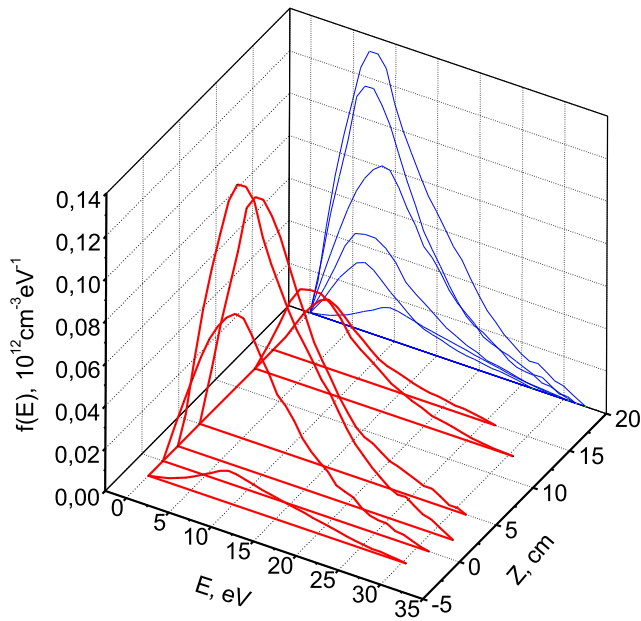
Figure 10. The electron energy distribution $f(E)$ at different distances along the axis at 40 μs of the discharge. The discharge parameters are the same as in figure 7. $U_{\text{an}} = 40$ V.

$0 < R < 2$ cm. There are high-frequency pulsations on the probe I–V characteristics, but their shape has a classical form. As a result of probe measurements, the axial distributions of U_{f} and U_{s} are obtained, which are similar to that observed in planar magnetrons.

Disturbances appear when the probe enters the ionization zone at $R > 2$ cm. On the ion current, they appear in the form of low-frequency ($T = 20$ μs) waves.

Figure 10 presents the EEDF $f(E)$ at different distances from magnetron along the discharge axis. High-energy electrons occupy a large space. The EEDF peak position shifts from 9 eV at $z = -2$ cm to 6 eV at $z = 15$ cm. The EEDF shows the presence of electrons with energy up to 32 eV. Thus, there are a large number of electrons with an energy above 11.3 eV capable of ionizing a carbon atom on the way from the target to the substrate.

For the electron impaction ionization, the mean ionization length λ_{iz} of the sputtered atom can be expressed as [12],

$$\lambda_{\text{iz}} = \frac{v_{\text{C}}}{k_{\text{iz}}n_{\text{e}}}, \tag{3}$$

where v_{C} is the velocity of the sputtered carbon atom and k_{iz} is the rate constant for electron impact ionization which is expressed as,

$$k_{\text{iz}} = k_0 e^{-E_0/T_{\text{e}}}. \tag{4}$$

The constants $E_0 = 12.6$ eV and $k_0 = 4 \times 10^{-8}$ cm^3 s^{-1} for carbon can be found in [12]. Using the Bohm flux formula can be estimated the ion density near the target:

$$j_{\text{e}} = 0.6en_{\text{e}}\sqrt{\frac{T_{\text{e}}}{M_{\text{Ne}}}}. \tag{5}$$

Then at $T_{\text{e}} = 9$ eV we obtain the ion density: $n_{\text{i}} = 1.5 \times 10^{13}$ cm^{-3}.

The probability of a C atom being ionized per unit distance (in this case 1 cm) at different locations can then be determined via equation (6) [33].

$$P_{\text{iz}}(z = 1) = 1 - \exp(-1/\lambda_{\text{iz}}). \tag{6}$$

The ionization probabilities P_{iz} can be determined using the measured T_{e} and n_{e} data. Inside the hollow cathode at $I_{\text{d}} = 160$ A, the plasma density is about 10^{13} cm^{-3} near the cylindrical surface. Discharge could be seen through the window at the far end of the chamber. Visually, the ionization zone near the cylindrical surface of the target has a thickness of about 10 mm. The mean ionization length λ_{iz} of the sputtered atom is of the order of 3 cm, assuming the most probable energy of sputtered carbon atoms of 3 eV. Then P_{iz} inside the hollow cathode is 0.28.

Outside the HCM for $n_{\text{e}} = 2 \times 10^{12}$ cm^{-3}, $T_{\text{e}} = 7$ eV and $v_{\text{C}} = 9 \times 10^4$ cm s^{-1} lead to $P_{\text{iz}} = 0.13$. Large values of P_{iz} are due to the high electron temperature. The use of Ne significantly increases the ionization of sputtered C compared to standard Ar-HiPIMS discharges, where a low ionization of C ($<5\%$) was observed [15].

In the HCM discharge with argon process gas the electron temperature is about 4 eV at pressure of 2.66 Pa. The discharge voltage reaches a stationary value of 500 V, which is independent of the initial applied voltage. The discharge voltage in argon is higher than the voltage in the discharge on neon, which can be explained by a higher coefficient of secondary electrons by neon ions [34]. The intensity of the C$^+$ (283.7 nm) is weakly distinguishable from noise at a pressure of 2.66 Pa and is noticeably manifested at a pressure of less than 1.33 Pa.

The plasma parameters are greatly exposed to the voltage at the anode ring U_{an}. Anode ring with an i.d. of 150 mm is made of a copper tube with a diameter of 8 mm. Measurements with a radial and axial probe showed that the plasma density increases throughout the volume when U_{an} on. The discharge current increases and the discharge voltage decreases by 20–30 V. The plasma and floating potentials also increase with growing U_{an}. Figure 11 shows the typical current–voltage characteristics of the probe at different voltages U_{an} on the anode ring at the same discharge currents and voltages. The plasma potential increases from -11 V to 8 V when the voltage U_{an} rises from 0 to 60 V. In addition, high-frequency pulsations appear on the probe characteristics with increasing U_{an}.

The cause of all of these events is to increase the electron temperature. Two phenomena are usually considered for an increase in the electron temperature: acceleration of secondary electrons in cathode sheath and Ohmic heating outside the cathode sheath. Due to the above-mentioned both of these methods do not work. The electron temperature increases due to instabilities. The electron route changes when a positive voltage is applied to the anode ring. In this case, most of them must move across the magnetic lines. Anomalous diffusion of electron is required to maintain a high current. Cross-field transport caused by collective phenomena such as plasma fluctuations and instabilities.
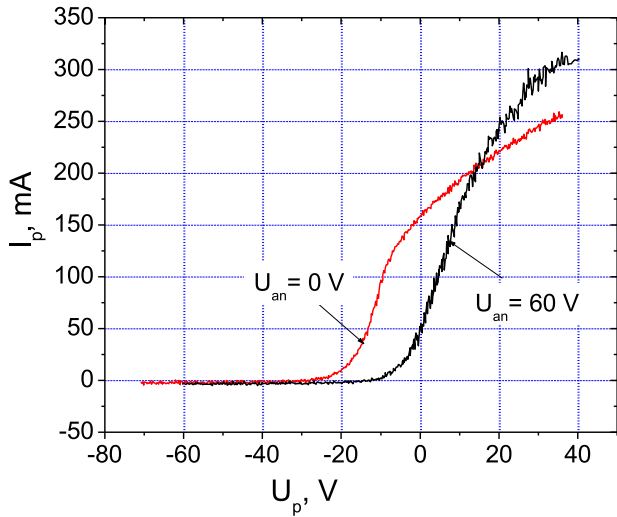
Figure 11. Typical probe current–voltage characteristic.

These instabilities increase the electron temperature by 1–2 V. As a result, the plasma density and the intensity of carbon ion lines also increase.

Carbon is the material with low sputtering yield and high ionization threshold. Figure 3(a) shows a linear increase in the current peak with growing applied voltage. This picture differs sharply from the current waveforms for a C target given by Anders *et al* for discharge in Ar with a C planar cathode, where the current jumped abruptly by a factor of 30 when the voltage was increased from 1100 V to 1150 V [35]. According to their assumption the only process that can explain the high current intensities in the discharge with the low self-sputtering yield materials is recycling of the process gas [36]. This model was further developed in the works [37, 38].

According to the generalized recycling model the discharge current consists of three parts:

$$I_{\mathrm{d}} \approx I_{\mathrm{i}} = I_{\mathrm{prim}} + I_{\mathrm{gas-recycle}} + I_{\mathrm{SS}}, \qquad (7)$$

where the primary current I_{prim} is defined by those atoms of the process gas, which are ionized for the first time, and then go to the target.

$I_{\mathrm{gas-recycle}}$ is produced by the flux of neutralized primary ions reflected from the target, which again ionize and participate in the creation of a discharge current.

I_{SS} stems the self-sputter recycling current of target atoms.

Anders *et al* was pointed out that I_{prim} has an upper limit I_{crit}, corresponding to the case where all incoming atoms from the surrounding gas reservoir are ionized and drawn to the target. The current density j_{crit} of background gas for a given conditions is determined by [36]:

$$j_{\mathrm{crit}} = e\left(\frac{2}{\pi m_{\mathrm{Ne}} k_{\mathrm{B}} T_{\mathrm{Ne}}}\right)^{1/2} \times p_{Ne} = 1.1 p_{Ne} (A\ cm^{-2}), \quad (8)$$

where m_{Ne}, p_{Ne} (Pa), $T_{\mathrm{Ne}} = 300$ K are the mass, pressure and temperature of the Ne gas respectively, e is the electron charge and k_{B} is the Bolzmann constant. Then for pressure $p = 2.66$ Pa

we get $j_{\mathrm{crit}} = 2.9$ A cm^{-2} which is more than $j_{\mathrm{i}} = 1.1$ A cm^{-2} in our discharge. Taking the racetrack area $S_{\mathrm{RT}} = 150$ cm^2 this gives the peak current that can be sustained solely by ionizing the available gas atoms:

$$I_{\mathrm{d}} = I_{\mathrm{crit}} + I_{\mathrm{SE}} \approx 1.1 I_{\mathrm{crit}} = 239\ \mathrm{A}, \qquad (9)$$

where I_{SE} is the current of secondary electrons.

Thus, the discharge was operated with no or little gas recycling.

Our experiments showed that the discharge works for hours without micro-arcing at pressures $p > 2.26$ Pa, currents $I_{\mathrm{d}} < 170$ A and pulse duration $\tau < 125$ μs.

Rare micro-arc formation occurs at a pressure $p < 1.86$ Pa, $I_{\mathrm{d}} > 160$ A and a discharge duration of more than 130 μs. But even then, a transition to runaway mode was not observed.

For comparison, we studied the HiPIMS discharge in neon with a planar carbon cathode. The cathode diameter is 90 mm. Preliminary measurements showed that at a distance of 9 cm, the plasma density is 10 times less compared to the HCM under the same pressure and power. The electron temperature is about 4 eV. The intensity of the C$^+$ (283.7 nm) line is also much lower.

The results presented above show that, in the HCM operating in pulsed mode, there are regions with a high electron temperature and densities of neon and carbon ions outside the hollow cathode. The ionization probability of thermalized carbon atoms is quite high under such conditions. The HCM allows to achieve a high density of carbon ions at current densities on the target below the critical, causing no occurrence of micro-arcs. An increase of the carbon ion fraction provides a possibility to improve the resulting DLC film properties.

4. Conclusion

In this work, we studied the properties of a Ne-HiPIMS discharge produced by a HCM with a graphite target. Using probe measurements, the plasma parameters inside and outside a HCM with average discharge power up to 490 W and pressure of 2.26 Pa have been determined. The peak plasma density on the discharge axis is located at a distance of 2–3 cm outside the magnetron. The electron density reaches 6×10^{12} cm^{-3} at distances of 2 cm and decreases to 1.5×10^{12} cm^{-3} at 12 cm at a power of 490 W. The electron temperature is 6 eV at a distance of 12 cm and increases to 9 eV inside the cathode. The high temperature and density of electrons in a large volume outside the hollow cathode increase the ionization probability of carbon atoms on their way from the target to the substrate. The optical emission spectroscopy at a distance of 12 cm from magnetron shows strong increase of the intensity ratio from C$^+$ ion and C neutral lines with the power. These measurements indicated large downstream ionization of sputtered copper atoms. The HCM showed that high currents and accordingly plasma densities can be achieved at low (400–500 V) discharge voltages. The probability of micro-arcs at the target decreases sharply at such voltages.

Acknowledgments

Data availability statement

All data that support the findings of this study are included within the article (and any supplementary files).

ORCID iDs

N P Poluektov ⬛ https://orcid.org/0000-0002-9589-892X

References

[1] Robertson J 2002 *Mater. Sci. Eng.* R **37** 129–281
[2] Erdemir A and Donnet C 2006 *J. Phys. D: Appl. Phys.* **39** R311
[3] Tillmann W, Vogli E and Hoffmann F 2009 *Surf. Coat. Technol.* **204** 1040
[4] Ferrari A C 2004 *Surf. Coat. Technol.* **180–181** 190
[5] Stüber M, Niederberger L, Danneil F, Leiste H, Ulrich S, Welle A, Marin M and Fischer H 2007 *Adv. Eng. Mater.* **9** 1114
[6] Panagiotopoulos N T, Patsalas P, Prouskas C, Dimitrakopulos G P, Komninou P, Karakostas T, Tighe A P and Lidorikis E 2010 *ACS Appl. Mater. Interfaces* **2** 3052
[7] Polo M C, Andújar J L, Hart A, Robertson J and Milne W I 2000 *Diam. Relat. Mater.* **9** 663–7
[8] Martin P J U and Bendavid A 2001 *Thin Solid Films* **394** 1–15
[9] Voevodin A A, Phelps A W, Zabinski J S and Donley M S 1996 *Diam. Relat. Mater.* **5** 1264–9
[10] Patsalas P, Kaziannis S, Kosmidis C, Papadimitriou D, Abadias G and Evangelakis G A 2001 *J. Appl. Phys.* **101** 124903
[11] Helmersson U, Lattemann M, Bohlmark J A, Ehiasarian A P and Gudmundsson J T 2006 *Thin Solid Films* **513** 1–24
[12] Hopwood J 1998 *Phys. Plasmas* **5** 1624–31
[13] Aijaz A and Kubart T 2017 *Appl. Phys. Lett.* **111** 051902
[14] Bugaev S P, Podkovyrov V G, Oskomov K V, Smaykina S V and Sochugov N S 2001 *Thin Solid Films* **389** 16–26
[15] DeKoven B M, Ward P R, Weiss R E, Christie R A, Scholl W, Sproul D, Tomasel F and Anders A 2003 *46th Annual Technical Conf. Proc.* vol 158 (Society of Vacuum Coaters)
[16] Sarakinos K, Braun A, Zilkens C, Mráz S, Schneider J M, Zoubos H and Patsalas P 2012 *Surf. Coat. Technol.* **206** 2706–10
[17] Fietzke F and Krätzschmar B-G 2014 *Thin Solid Films* **572** 147–52
[18] Ganesan R, McCulloch D G, Marks N A, Tucker M D, Partridge J G, Bilek M M M and McKenzie D R 2015 *J. Phys. D: Appl. Phys.* **48** 442001
[19] Konishi T, Yukimura K and Takaki K 2016 *Surf. Coat. Technol.* **286** 239
[20] Aijaz A, Sarakinos K, Lundin D, Brenning N and Helmersson U 2012 *Diam. Relat. Mater.* **23** 1–4
[21] Aijaz A, Ferreira F, Oliveira J and Kubart T 2018 *Coatings* **8** 385
[22] Lundin D, Čada M and Hubička Z 2015 *Plasma Sources Sci. Technol.* **24** 035018
[23] Tsar'gorodsev Y P, Poluektov N P, Usatov I I, Evstigneev A G, Kozlovskaya E P and Amelkin O O 2019 *Plasma Phys. Rep.* **45** 592
[24] Chen F F 1965 *Plasma Diagnostic Techniques* ed R H Huddlestone and S L Leonard (New York: Academic) p 113
[25] Vyas V and Kushner M J 2006 *J. Vac. Sci. Technol.* A **24** 1955
[26] Vitelaru C, Lundin D, Stancu G D, Brenning N, Bretagne J and Minea T 2012 *Plasma Sources Sci. Technol.* **21** 025010
[27] Poluektov N P, Tsar'gorodsev Y P, Usatov I I, Evstigneev A G and Kamyschov I A 2015 *Plasma Sources Sci. Technol.* **24** 035009
[28] Macák K, Kouznetsov V, Schneider J, Helmersson U and Petrov I 2000 *J. Vac. Sci. Technol.* A **18** 1533
[29] Vetushka A and Ehiasarian A P 2008 *J. Phys. D: Appl. Phys.* **41** 015204
[30] Vlček J, Pajdarova A D and Musil J 2004 *Contrib. Plasma Phys.* **44** 426
[31] Poluektov N P, Tsar'gorodsev Y P, Usatov I I, Evstigneev A G and Kamyschov I A 2012 *J. Mod. Phys.* **03** 1494
[32] Vyas V and Kushner M J 2006 *J. Vac. Sci. Technol.* A **24** 1955–69
[33] Chapman B 1980 *Glow Discharge Processes: Sputtering and Plasma Etching* (New York: Wiley)
[34] Baragiola R A, Alonso E V, Ferron J and Oliva-Florio A 1979 *Surf. Sci.* **90** 240
[35] Anders A, Andersson J and Ehiasarian A 2007 *J. Appl. Phys.* **102** 113303
[36] Anders A, Čapek J, Hála M and Martinu L 2012 *J. Phys. D: Appl. Phys.* **45** 012003
[37] Huo C, Lundin D, Raadu M A, Anders A, Gudmundsson J T and Brenning N 2014 *Plasma Sources Sci. Technol.* **23** 025017
[38] Brenning N, Gudmundsson J T, Raadu M A, Petty T J, Minea T and Lundin D 2017 *Plasma Sources Sci. Technol.* **26** 125003